International Journal of Nanomedicine

Dovepress

open access to scientific and medical research

Open Access Full Text Article

ORIGINAL RESEARCH

Preparation of Hematoporphyrin-Poly(Lactic Acid) Nanoparticles Encapsulated Perfluoropentane/Salicylic Acid for Enhanced US/CEST MR Bimodal Imaging

Liqiong Ding[1,*], Fengnan Xu[1,*], Binhua Luo[1,*], Liyuan Cheng[1], Lingping Huang[2], Yanlong Jia[3], Jieqiong Ding[1]

[1]Xianning Medical College, Hubei University of Science and Technology, Xianning, Hubei Province, People's Republic of China; [2]Department of Medical Ultrasound, Xianning Central Hospital, The First Affiliated Hospital of Hubei University of Science and Technology, Xianning, Hubei Province, People's Republic of China; [3]Department of Radiology, Xiangyang Central Hospital, Affiliated Hospital of Hubei University of Arts and Science, Xiangyang, Hubei Province, People's Republic of China

*These authors contributed equally to this work

Correspondence: Yanlong Jia, Department of Radiology, Xiangyang Central Hospital, Affiliated Hospital of Hubei University of Arts and Science, Xiangyang, Hubei Province, 441021, People's Republic of China, Tel +86 13669006180, Email yanlongjia@163.com; Jieqiong Ding, Xianning Medical College, Hubei University of Science and Technology, Xianning, Hubei Province, 437100, People's Republic of China, Tel +86 13797244300, Email djq197911@163.com

Background: Medical imaging modalities, such as magnetic resonance imaging (MRI), ultrasound, and fluorescence imaging, have gained widespread acceptance in clinical practice for tumor diagnosis. Each imaging modality has its own unique principles, advantages, and limitations, thus necessitating a multimodal approach for a comprehensive disease understanding of the disease process. To enhance diagnostic precision, physicians frequently integrate data from multiple imaging modalities, driving research advancements in multimodal imaging technology research.

Methods: In this study, hematoporphyrin-poly (lactic acid) (HP-PLLA) polymer was prepared via ring-opening polymerization and thoroughly characterized using FT-IR, ^{1}H-NMR, XRD, and TGA. HP-PLLA based nanoparticles encapsulating perfluoropentane (PFP) and salicylic acid were prepared via emulsion-solvent evaporation. Zeta potential and mean diameter were assessed using DLS and TEM. Biocompatibility was evaluated via cell migration, hemolysis, and cytotoxicity assays. Ultrasonic imaging was performed with a dedicated apparatus, while CEST MRI was conducted using a 7.0 T animal scanner.

Results: We designed and prepared a novel dual-mode nanoimaging probe SA/PFP@HP-PLLA NPs. PFP enhanced US imaging, while salicylic acid bolstered CEST imaging. With an average size of 74.43 ± 1.12 nm, a polydispersity index of 0.175 ± 0.015, and a surface zeta potential of −64.1 ± 2.11 mV. These NPs exhibit excellent biocompatibility and stability. Both in vitro and in vivo experiments confirmed the SA/PFP@HP-PLLA NP's ability to improve tumor characterization and diagnostic precision.

Conclusion: The SA/PFP@HP-PLLA NPs demonstrate promising dual-modality imaging capabilities, indicating their potential for preclinical and clinical use as a contrast agent.

Keywords: contrast agent, perfluoropentane, salicylic acid, ultrasound imaging, chemical exchange saturation transfer

Introduction

Cancer poses a significant threat to human health, with annual global statistics showing approximately 19 million new diagnoses and over 10 million deaths. Early detection and intervention are crucial for improving treatment outcomes and survival rates. However, tumor removal poses numerous challenges due to its aggressive nature, rapid growth, high heterogeneity, and indistinguishable boundaries from healthy tissue.[1] These complexities underscore the need for

Received: 12 December 2023
Accepted: 7 May 2024
Published: 21 May 2024

advanced real-time diagnosis and therapeutic techniques that can precisely define tumor boundaries, guide surgical resections, and detect any residual tumor cells.[2,3]

In recent decades, medical imaging technology has undergone remarkable advancements, with multimodality imaging emerging as a particularly valuable tool in the early diagnosis, treatment monitoring, and prognosis of various diseases. Among these imaging types, ultrasound stands out for its non-invasiveness, low radiation exposure, cost-effectiveness, and real-time capabilities.[4] Ultrasound contrast imaging involves the injection of contrast agents into the bloodstream, which enhances the scattered echoes and improves the contrast between tissues and blood vessels in ultrasound images. This technique not only enhances image resolution but also broadens the scope and depth of ultrasound applications.[5,6] However, traditional ultrasound contrast agents, typically in the micron size range, have limitations such as short circulation times and difficulties in extravascular visualization due to their larger size. These agents are primarily suitable for vascular imaging rather than tumor visualization.[7] To overcome the limitations of traditional ultrasound contrast agents, recent focus has shifted towards nanomaterials,[8,9] particularly polymer-based ones, due to their distinct physicochemical characteristics, biocompatibility, low toxicity, and encapsulation capabilities.[10–14] These nanomaterials can integrate multiple functions, such as drug delivery and photothermal therapy, offering great potential for enhancing diagnosis accuracy and treatment efficacy in cancer therapy. Perfluoropentane (PFP) is a particularly promising class of ultrasound contrast agents for cancer therapy due to its small droplet size, excellent stability, and acoustic properties, as well as its ability to undergo phase transition under ultrasound excitation.[15–19]

Magnetic Resonance Imaging (MRI) is a crucial clinical tool for tumor visualization, offering high sensitivity. This sensitivity is further enhanced by Diffusion-Weighted Imaging (DWI) and Dynamic Contrast-Enhanced Scan (DCE), which provide detailed analysis of tumor tissue composition and blood supply. Chemical Exchange Saturation Transfer (CEST) MRI, introduced by Ward et al in 2000,[20] utilizes magnetization transfer (MT) to indirectly detect molecules within the micromolar to the millimolar range.[21–23] CEST imaging involves applying radiofrequency saturation pulses to exchangeable protons in molecular structures, exciting them and facilitating their exchange with hydrogen protons in surrounding water molecules. By monitoring the reduction in free water signals, physiologically and biochemically relevant tissue information can be obtained.[24–27] CEST contrast agents are divided into paramagnetic and diamagnetic categories. Paramagnetic agents, typically metal chelates, offer chemical shifts and low background interference but may pose metal toxicity risks.[28] In contrast, diamagnetic agents, organic molecules with exchangeable protons, avoid metal-based toxicities. Salicylic acid (SA), a key aspirin component, resonates with water at 9.3 ppm due to hydrogen bonding, making it an ideal CEST contrast agent.[29]

The integration of ultrasound with CEST MRI in multimodality imaging has the potential to greatly improve tumor visualization. To this end, we successfully synthesized HP-PLLA, a star-structured polylactic acid (S-PLLA), using ring-opening polymerization, and prepared nanoparticles encapsulating PFP and salicylic acid.[30–32] Figure 1 illustrates the

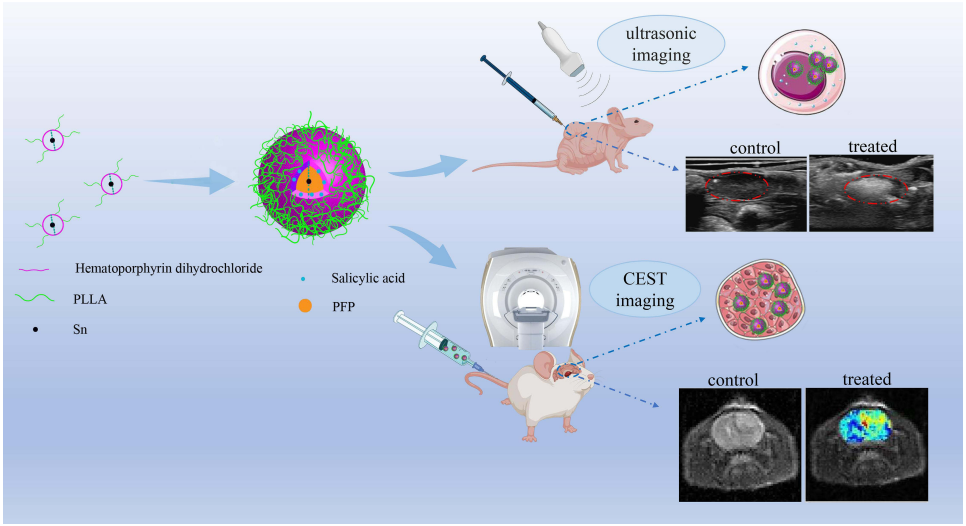

Figure 1 The schematic diagram of SA/PFP@HP-PLLA NPs as a dual-modality imaging contrast agent.

preparation of SA/PFP@HP-PLLA cross-ester nanoparticles using the emulsion-solvent evaporation method. These NPs function as a dual-modality imaging contrast agent, enhancing the visualization of tumor boundaries, resection areas, and residual tumors. Their exceptional biocompatibility, stability, and imaging signal amplification abilities render them a promising candidate for preclinical and clinical applications.

Materials and Methods

Materials and Reagents

Hematoporphyrin (HP) and $Sn(Oct)_2$ were obtained from Shanghai Aladdin Biochemical Technology Co., Ltd. (Shanghai, China). L-lactide was purchased from Daigang Biotechnology Co., Ltd. (Shandong, China). PFP was procured from Jenkem Technology Co., Ltd. (Beijing, China). Chloroform ($CHCl_3$), absolute alcohol, span 80, and sodium dodecyl sulfate (SDS) were obtained from Sinopharm Chemical Reagent Co., Ltd. (Shanghai, China). CCK-8 kits were purchased from Wuhan Kerui Biotechnology Co., Ltd. (Wuhan, China). All other reagents were analytically pure.

Synthesis of HP-PLLA Polymer

The preparation of the HP-PLLA polymer was carried out through a ring-opening polymerization reaction. L-lactide (recrystallized with ethyl acetate, 30 mmol) was mixed with HP (20.0 mg, 0.030 mmol) and $Sn(Oct)_2$ (12 mg, 0.075 mmol) in a 50 mL three-necked round-bottom flask. The mixture was then heated to 120°C and reacted under a pure nitrogen atmosphere for 2 hours. The crude product was cooled to room temperature and dissolved in an appropriate amount of dichloromethane. The solution was then precipitated in cold deionized water and washed three times. Finally, the product was dried under vacuum to obtain the polymer. The synthesis route is shown in Figure 2.

Characterization Techniques of HP-PLLA Polymer

The samples were characterized using Fourier transform infrared spectroscopy (FTIR), ^{1}H-nuclear magnetic resonance (^{1}H-NMR) spectroscopy, X-ray diffraction (XRD), and thermogravimetric analysis (TGA). The FTIR spectra were acquired using an AFFINITY-1 FTIR spectrophotometer (Shimadzu, Japan) in the 4000–500 cm^{-1} range with KBr pellets. The ^{1}H-NMR spectra was recorded using a Bruker Avance III 400 nuclear magnetic resonance spectrometer (Brook, Switzerland) for qualitative structure analysis. XRD patterns were obtained from an XRD-6100 diffractometer (Shimadzu, Japan) at room temperature with the following parameters: Cu target, voltage 40 kV, current 30 mA, scan speed 10 deg/min, and scan range 10°~80°. TGA was carried out using a TG209F3 Thermo Gravimetry (Netzsch, Germany) from 100°C to 600°C at a heating rate of 10°C /min in a nitrogen atmosphere.

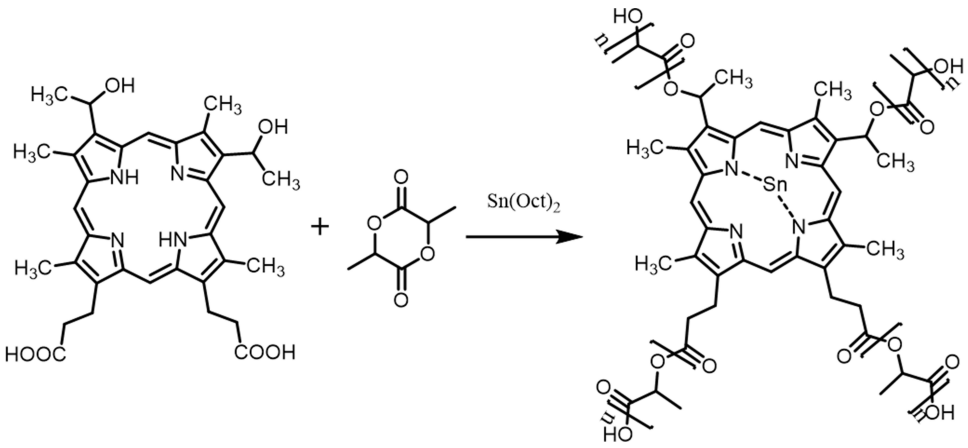

Figure 2 The synthesis route of HP-PLLA polymer.

Preparation of SA/PFP@HP-PLLA NPs

SA/PFP@HP-PLLA NPs were prepared by the emulsion-solvent evaporation method using the following steps: 30.0 mg of SA was dissolved in 0.5 mL of anhydrous ethanol and dispersed in 1 mL of chloroform containing 50.0 mg of HP-PLLA polymer. 2~3 drops of Span 80 were added, and stirring was continued to obtain a homogeneous solution. A primary emulsion was formed by stirring the mixed solution at 10,000 rpm for 2~3 minutes at ice bath temperature after adding 0.5 mL of PFP. The resulting emulsion was rapidly dropped into 5 mL of 0.5% sodium dodecyl sulfate solution (SDS) and ultrasonically treated in an ice bath with an ultrasonic cell disruptor for 5 minutes. The double emulsion obtained was gently stirred at room temperature for 24 hours to obtain the SA/PFP@HP-PLLA NPs.

Characterization of the SA/PFP@HP-PLLA NPs

The average particle size and surface potential of SA/PFP@ HP-PLLA NPs were measured using a Malvern Laser Particle Size Analyzer (Zetasizer Nano ZSE), confirming the successful formation of these nanoparticles. To evaluate their storage stability, the samples were stored in a refrigerator at 4°C and withdrawn at specific intervals (0, 5, 10, 15, 20, and 30 days). Furthermore, the morphology of SA/PFP@HP-PLLA NPs was observed using a Transmission Electron Microscope (TEM, Tokyo, Japan).

Cell Culture

The rat C6 glioma (C6) cell line was provided by the Shanghai Institute of Life Science Cell Resource Center (Shanghai, China). C6 cells were cultured in a medium Dulbecco's Modified Eagle's Medium (DMEM) supplemented with 10% fetal bovine serum (FBS) and 1% penicillin-streptomycin in a cell incubator maintained at 37°C and 5% CO_2.

Cytotoxicity Test

The Cell Counting Kit-8 (CCK-8) assay was used to assess the cytotoxicity of HP-PLLA on rat C6 glioma cells. C6 cells were seeded at a density of 5×10^6 cells/well in a 96-well plate containing DMEM supplemented with 10% FBS and incubated in a conventional cell culture incubator for 24 hours. Subsequently, the culture medium was aspirated, and fresh culture medium containing different concentrations of HP-PLLA (1.0, 0.75, 0.5, 0.25, 0.05 μg/μL) was added, followed by incubation for another 24 hours. The old culture medium was discarded, and 100 μL of DMEM containing 10% CCK-8 was added to each well, followed by further incubation for 1 hour. The absorbance was measured at 450 nm with a microplate reader, and the cell survival rate was calculated according to the following equation:

$$\text{Cell viability rate} = \frac{A_s - A_b}{A_c - A_b} \times 100\%$$

where, A_s represents the absorbance of the experimental group, A_b represents the absorbance of the blank group, A_c represents the absorbance of the control group.

Cell Migration Assay

The cell scratch method is a technique used to assess the migration movement and repair capacity of cells. Briefly, C6 cells were seeded into 6-well plates at a density of 6~8 $\times10^5$ per well and allowed to adhere overnight in a conventional cell culture incubator. Once the cells achieved a confluence of greater than 90%, as observed under an inverted microscope (Olympus, Japan), a sterile pipette tip was used to introduce a straight-line scratch across the cell monolayer. Debris was removed by washing with sterile PBS, and various concentrations of HP-PLLA were added to the culture medium (DMEM containing 2% FBS) for 24 hours. Images of cell migration were captured under an inverted microscope. The images were analyzed and processed using Image J software. Each experiment was repeated three times, and the migration rate was calculated according to the following formula:

$$\text{Migration rate} = \left[\frac{(A_0 - A_t)}{A_0}\right] \times 100\%$$

Where, A_0 represents the initial area and A_t represents the area at a specific time point.

Hemolysis

Hemolysis is a process where red blood cells rupture, releasing their contents into the surrounding fluid. It can be induced by various agents, including certain chemicals and materials. To assess the hemolytic potential of HP-PLLA, which was mixed with a red blood cell suspension (2%, V/V) to create cell suspensions with varying concentrations (1.0, 0.75, 0.5, 0.25, 0.05 μg/μL). The negative control group consisted of a mixture of normal saline and red blood cell suspension (1:1, V/V), while the positive control group was a mixture of double distilled water and red blood cell suspension (1:1, V/V). These mixtures were incubated at 37°C for 1 hour. Subsequently, they were centrifuged at 1000 rpm for 5 minutes at 4°C. The supernatant was then transferred to a 96-well plate, and its absorbance was measured at 540 nm by a spectrophotometer. The hemolysis rate was calculated according to the following formula:

$$\text{Hemolysis ratio} = \left[\left(A_{\text{sample}} - A_{\text{negative}}\right)/\left(A_{\text{positive}} - A_{\text{negative}}\right)\right] \times 100\%$$

Animal Care

All animal care and experiments were conducted in according to the Guidelines of Animal Experimentation of Hubei University of Science and Technology and the National Institute of Health. The study protocol was approved by the Institutional Animal Care and Use Committee of Hubei University of Science and Technology (approval number: 2022–0024).

Blood Biochemistry Analysis

For blood biochemistry analysis, Zealand White rabbits weighing 2.5~3.0 kg were utilized for in vivo toxicity evaluation. First, rabbits were placed on a dissection table, and heart blood samples (2 mL) were collected using heparin-wetted EP tubes as the control group. Then, a certain dose of SA/PFP@HP-PLLA NPs was administered intravenously through the rabbits' ear marginal vein. On the third and seventh days after injection, heart blood sampling (2 mL) was repeated. Liver and kidney indices were measured using a fully automated blood biochemistry analyzer. Liver indices mainly included total protein [TP], albumin [ALB], globulin [GLB], alanine aminotransferase [ALT], and aspartate aminotransferase [AST]. Renal indicators were mainly blood urea nitrogen [BUN] and creatinine [CRE]).

Ultrasound Imaging

To assess the imaging effect of SA/PFP@HP-PLLA NPs, an ultrasonic imager with a 10 MHz probe was used. A solution of SA/PFP@HP-PLLA NPs was added to latex gloves, the air removed, the gloves sealed, and then soaked in a constant temperature water bath. The ultrasonic images were collected with the probe in contact with the gloves coated with ultrasonic medical-coupled gel at different temperatures. The same method was used to obtain ultrasonic images of normal saline and ultrasonic medical coupling gel in a 37°C constant temperature water bath as a control. All contrast images were captured utilizing B-mode imaging, which maintained a consistent frame rate of 51 Hz, a mechanical index set to 1.1, a gain adjustment of 44%, a dynamic range of 60 dB, and a low level of persistence throughout the recording process.

For in vivo imaging, C6 cells in the logarithmic growth phase were processed to create a single cell suspension. These cells were injected into the subcutaneous area of male BALB/C nude mice to establish a subcutaneous tumor model. Once the tumors reached a diameter of approximately 1.0 cm, the mice were anesthetized and placed on a heating plate. Ultrasound pharmacological coupling gel was applied to the tumor surface, and ultrasound images were acquired as a control. Subsequently, SA/PFP@HP-PLLA NPs (150 μL) were injected directly into the tumor, and additional ultrasound images were captured with the same instrument parameters.

CEST MRI

For in vitro CEST imaging, a subset of samples were taken for acid-base adjustment and subsequently placed into test tubes before being scanned using a 7.0T MRI scanner. The specific scanning parameters were as follows: **T2-weighted anatomical images**: Repletion Time (TR) = 4000 ms, Echo Time (TE) = 10 ms, Field of view (FOV) = 30 mm × 30 mm, slice thickness = 2.0 mm, slice spacing = 0 mm, matrix size = 128 × 128, average acquisitions (Averages, AV) = 4,

segments/ETL = 16/8, Kzero = 4. **B_0 map**: TR = 40 ms, TE = 3 ms, 3.5 ms, 4 ms, slice thickness = 2 mm, FOV = 30 mm × 30 mm, matrix size = 64 × 64, flip angle (FA) = 15°, averages = 12. **EPI-CEST sequence**: selected at the same level as the B0 map, TR = 6000 ms, TE = 29.46 ms, Kzero = 32, slice thickness = 2 mm, FOV = 30 mm × 30 mm, matrix size = 64 × 64, the total scan time of 10 minutes 37 sec.

In vivo CEST imaging, the rat glioma model was prepared by referring to the literature method of Luo et al.[33] Wistar male rats weighing about 250 g were anesthetized with 10% chloral hydrate (4 mL/kg) intraperitoneally and fixed on a brain stereotaxic apparatus. Glioma cells were inoculated into the right frontal lobe of the rat brain by drilling a craniotomy 3 mm lateral to the sagittal suture and 1 mm posteriorly. A 25-μL microinjector was used to slowly inject 10 μL (1×10^6) of C6 cell suspension at a rate of 1 μL/min. About 14 days past, MRI was used to confirm the successful modeling of tumor-bearing rats.

Tumor-bearing rats were anesthetized with isoflurane (4% for induction, 2.0–2.5% for maintenance, in a 5% O_2 oxygen flow), and 1.5 mL of SA/PFP@HP-PLLA NPs solution was injected from the tail vein. During MRI experiments, the respiratory rate and amplitude were monitored in real-time using a small animal cardiac monitor (SAII Technologies, USA). The tumor was placed right in the center of the magnet for optimal imaging. B_0 map and B_1 map should be acquired before the experiment to eliminate the interference of magnetic field inhomogeneity on the signal. **B_0 map**: TR = 40 ms, TE = 3, 3.5, 4 ms, slice thickness = 4 mm, FOV = 25×25 mm, matrix = 64 × 64, FA= 15°, averages = 12. **B_1 map**: TR = 8000 ms, TE = 11.37 ms, slice thickness = 4 mm, FOV = 40 mm × 40 mm, matrix = 64 × 64, flip angle = 60°, 120°. **T2WI anatomical images**: TR = 4000 ms, TE = 10 ms, slice thickness = 2 mm, slice spacing = 0 mm, FOV = 40 mm × 40 mm, matrix = 128 × 128, segments/ETL = 16/8, Kzero = 4. **EPI-CEST**: TR = 6000 ms, TE = 27.63 ms, thickness = 4 mm, FOV = 40×40 mm, matrix = 64 × 64, ETL = 64, Kzero = 32, shots = 1, repetitions = 1, averages = 1, dummy scans = 7. The total scan time was 13 minutes and 13 seconds.

Data Analysis

CEST image processing was performed on the MATLAB (MathWorks, Natick, MA, USA, Matlab 2011b) platform using a post-processor script edited by our experimental engineers. The magnitude of the CEST effect, also known as magnetization transfer ratio (MTRasym) was primarily measured using the following equation:

$$MTR_{asym} = \frac{S(-\Delta\omega) - S(+\Delta\omega)}{S_0}$$

Where S(-Δω) and S(+Δω) were the signal intensity of free water when selective saturation pulses were applied at -Δω and +Δω frequencies, respectively, and S_0 was the signal intensity of free water in the absence of selective saturation pulses.

Results and Discussion

Characterization of HP-PLLA Polymer

The prepared HP-PLLA, PLLA and HP were characterized by infrared spectroscopy. As shown in Figure 3, the HP possessed the porphyrin-ring related bands at 1639 cm^{-1}, the bands at 3049 cm^{-1} were attributed to -N-H in porphyrin-ring, the bands at 1720 cm^{-1} and 3370 cm^{-1} could be attributed to the C=O stretching vibration in the carboxyl groups and the -O-H stretching vibration. The obvious absorption of PLLA at 1757 cm^{-1} belonged to the C=O stretching vibration, the strong bands at 1083 cm^{-1} and 1125 cm^{-1} belonged to the stretching vibration of lactone C-O chain, the stretching vibration of methyl appeared at 2991 cm^{-1} and 2948 cm^{-1}, and there were weak and sharp free hydroxyl absorption peaks at 3509 cm^{-1}. The presence of characteristic peaks of HP and PLLA in the FTIR spectrum confirmed its successful preparation. Additionally, comparing the infrared spectrum of HP-PLLA with that of HP, the disappearance of -N-H stretching vibration bands at 3049 cm^{-1} indicated Sn(II) coordination with -N-H groups, further validating the preparation of HP-PLLA polymer.

The molecular structure of synthesized HP-PLLA was further characterized using ^{1}H-NMR spectroscopy. As shown in Figure 4, the introduction of the initiator HP caused shifts in the chemical shift peaks of PLLA. Specifically, the peaks at δ = ~5.21 ppm and ~1.53~1.61 ppm were attributed to the proton absorption of the methine and methyl groups in the

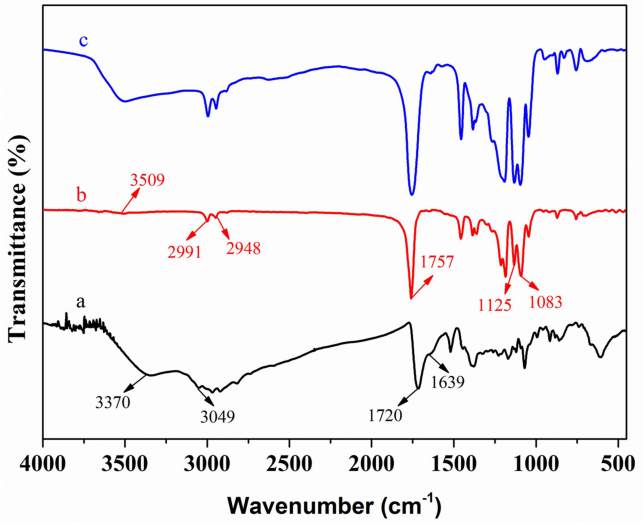

Figure 3 FTIR spectrum of HP (a), PLLA (b), HP-PLLA (c).

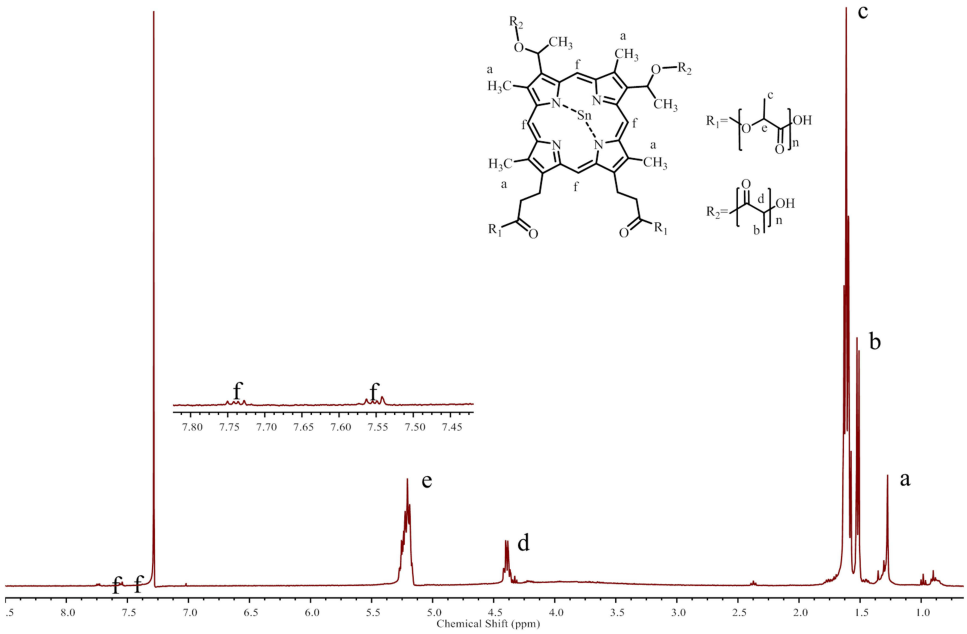

Figure 4 Proton nuclear magnetic resonance spectra (in $CDCl_3$, ppm) of HP-PLLA polymer.

repeating unit of the chain structure, respectively. Additionally, the peak at δ = 4.39 ppm was attributed to the absorption peak of the submethyl proton at the hydroxyl end. Notably, a novel chemical shift peak appeared at δ = ~7.55~7.75 ppm, which was distinct from the chemical shift of HP's molecular structure. This peak was inferred to be the proton absorption peak of the metal tin atom of the catalyst stannous octoate coordinated with the porphyrin to generate the metal porphyrin. The absence of an N-H shift peak for the two pyrroles of the porphyrin ring near ~2.9 ppm further supported this inference. Collectively, these observations offered compelling evidence for the successful preparation of HP-PLLA through the coordination of porphyrin and metal tin atoms.

XRD is a valuable technique for analyzing the crystal structure of materials by examining the diffraction patterns resulting from the interaction of X-rays with the atomic lattice of crystals. Figure 5 displays the XRD patterns of PLLA and HP-PLLA. Pure PLLA exhibited distinct diffraction peaks at 2θ=16.7° and 19.0°, which corresponded to the (200)

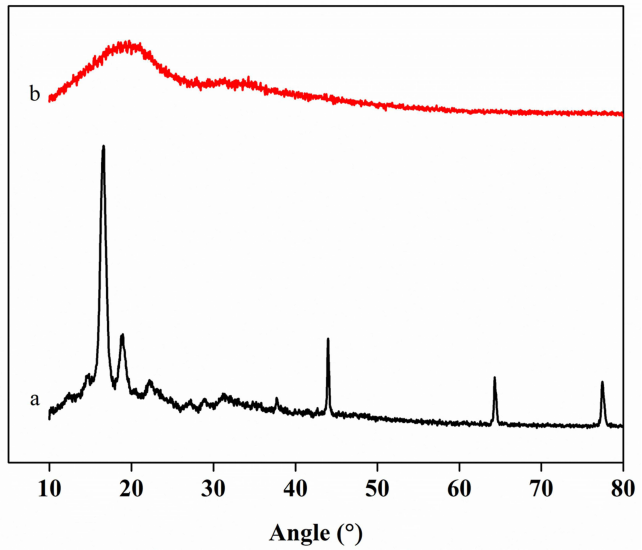

Figure 5 X-ray diffraction pattern of PLLA (a) and HP-PLLA (b).

and (203) crystal planes of α'crystal form, belonging to the orthorhombic crystal system. The other characteristic diffraction peaks were observed at 2θ=14.6°, 22.4°, 43.8°, 64.4° and 77.6°, corresponding to (010) crystal plane and (205) crystal plane, respectively. When compared to the XRD pattern of PLLA, the XRD pattern of HP-PLLA displayed a widely diffuse crystal plane diffraction peak without any other notable absorption peaks, suggesting that the crystal structure of PLLA was disrupted and an amorphous structure was formed. This finding further validated the successful preparation of HP-PLLA.

The thermal stability of HP and HP-PLLA were evaluated using TGA, as shown in Figure 6. The decomposition of PLLA started at approximately 134°C. However, HP-PLLA delayed this process to around 157°C. This observation indicated that the introduction of HP had enhanced the thermal stability of PLLA. Additionally, previous studies have reported that the pyrolysis temperature of HP to be 180°C.[34] The pyrolysis temperature of HP-PLLA polymer was found to be between HP and PLLA, consistent with the thermal stability trend of copolymers. These results confirmed the improved thermal stability of PLLA in the presence of HP.

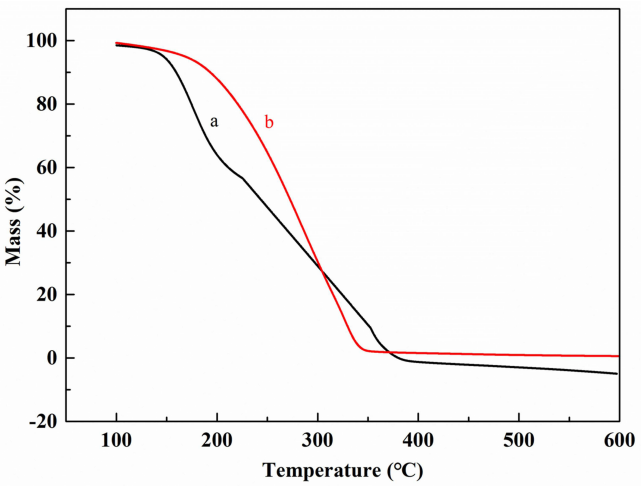

Figure 6 Thermogravimetric analysis chart of PLLA (a) and HP-PLLA (b).

Characterization of SA/PFP@HP-PLLA NPs

The preparation of SA/PFP@HP-PLLA NPs presented as phenol red and opalescence suspensions, as shown in Figure 7a. The average size of the prepared nanoparticles was 74.43 ± 1.12 nm Figure 7b, with a polydispersity index of 0.175 ± 0.015 and an average surface zeta potential of −64.1 ± 2.11 mV Figure 7c. These values indicate a narrow size distribution and a relatively uniform population of NPs. The nanoparticles were observed to be spherical and uniformly dispersed on TME, as depicted in Figure 7d. To examine the stability of the SA/PLLA-HP NPs, they were stored at 4°C for 30 days and their particle size and potential changes were measured. The results, shown in Figure 7e, indicated that the particle size and potential of the nanoparticles remained relatively stable during the storage period (0, 5, 10, 20, and 30 days), suggesting that SA/PFP@HP-PLLA NPs had good stability under low-temperature conditions. Overall, the SA/PFP@HP-PLLA NPs exhibited desirable characteristics, including uniform spherical morphology, a narrow size distribution, a high negative zeta potential, and good stability under low-temperature conditions.

Cytotoxicity Assay and Hemolysis

To investigate the in vitro cytotoxicity of HP-PLLA, the cell viability of C6 cells incubated with HP-PLLA at different concentrations was evaluated using the CCK-8 assay. As the concentration of HP-PLLA increased, there was no significant change ($p > 0.05$) in the vitality of C6 cells after incubation for 24 hours, indicating that HP-PLLA had

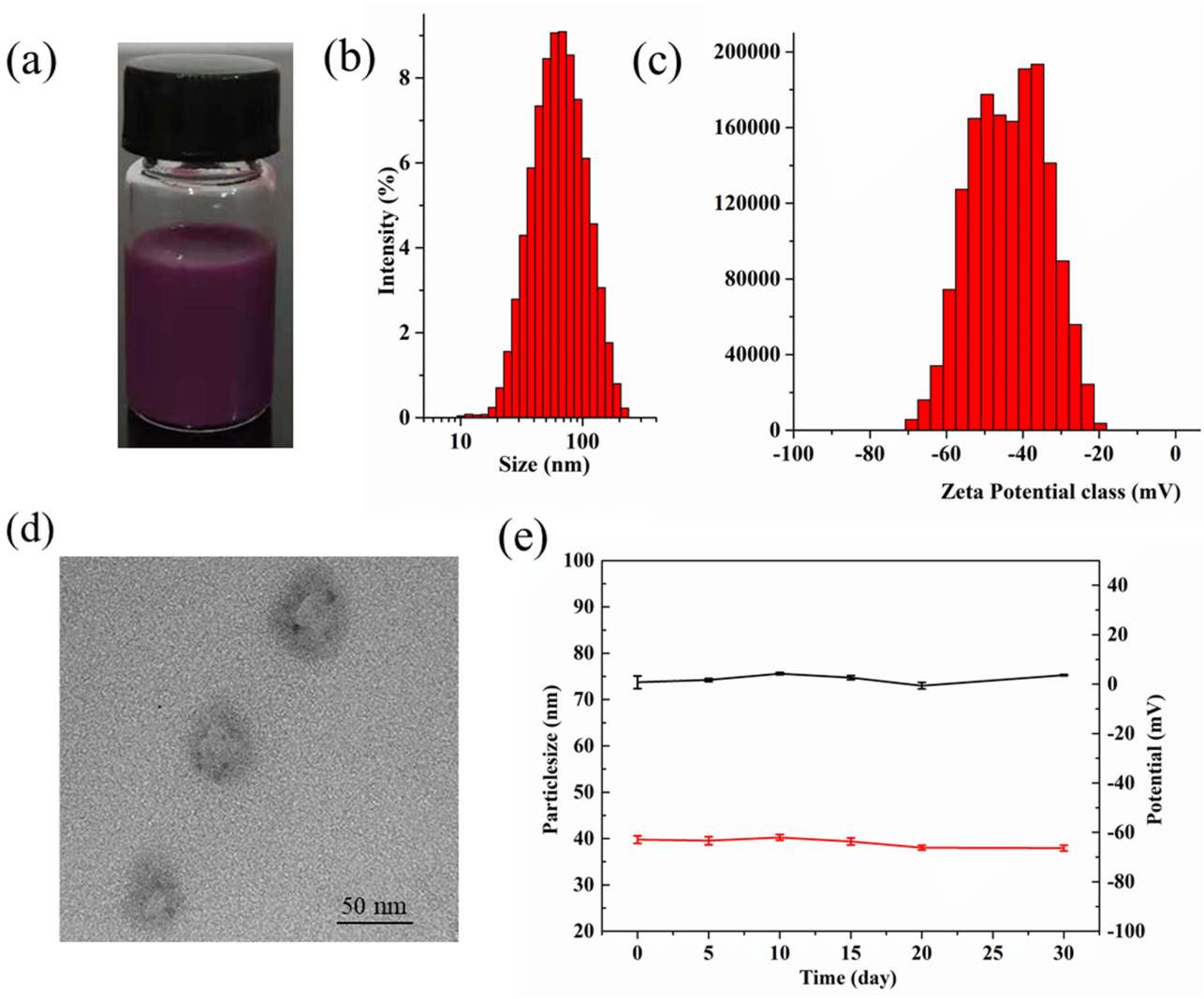

Figure 7 Characterization of SA/PFP@HP-PLLA NPs. (**a**) digital photo, (**b**) size distribution, (**c**) zeta potential, (**d**) TEM images, and (**e**) stability of the NPs in vitro.

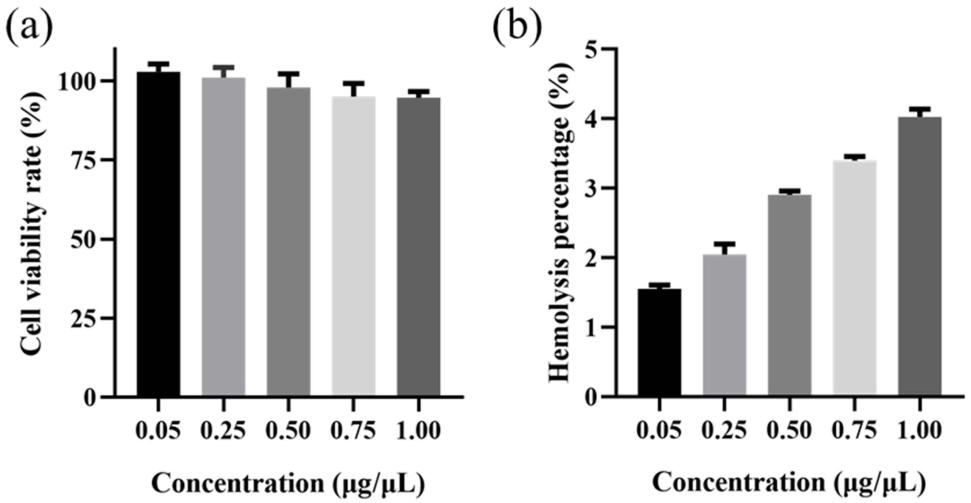

Figure 8 Cytotoxicity assay and Hemolysis of HP-PLLA. (**a**) presents the cytotoxicity assessment using the CCK-8 assay, reporting the mean ± SD (n = 5) of the in vitro cell viability of C6 cell incubated with HP-PLLA at varying concentrations for 24 hours. (**b**) demonstrates the in vitro hemolysis experiment, exhibiting the mean ± SD (n = 5) of the hemolysis rate of erythrocyte suspensions incubated with HP-PLLA.

minimal toxicity to C6 cells, as shown in Figure 8a. Additionally, the hemolysis rate of HP-PLLA at different concentrations was less than 5%, as presented in Figure 8b.

Cell Migration Assay

In this study, the scratch assay was used to investigate the effect of HP-PLLA on the migration rate of C6 cells. After 24 hours of incubation with C6 cells at different experimental concentrations (0.25, 0.50, 0.75, 1.00 μg/μL), the effect of cell migration was observed. As shown in Figure 9, there was no significant difference in the migration rate between the control group (without HP-PLLA) and experimental groups (0.25, 0.50, 0.75, 1.00 μg/μL). Specifically, the migration rates were 86.85 ± 1.00%, 86.26 ± 1.35%, 83.47 ± 1.29%, 82.98 ± 0.93%, and 80.93 ± 1.80%, respectively, as shown in Figure 10. Statistical analysis (n = 3)

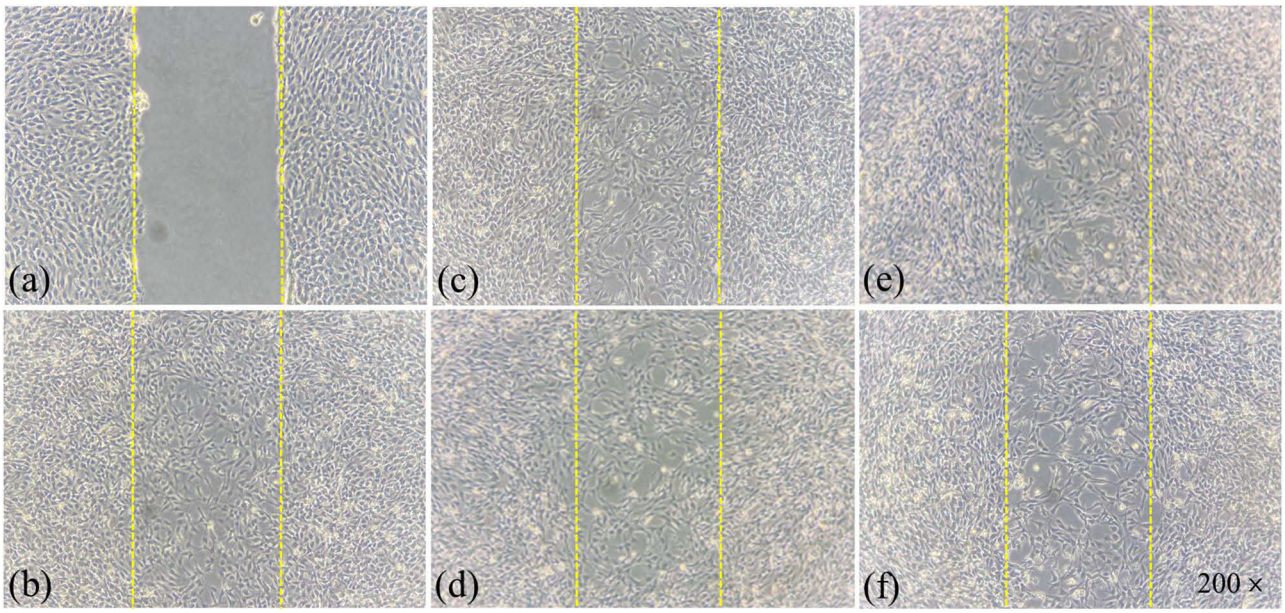

Figure 9 Effects of HP-PLLA on the migration of C6 cells. (**a**) represents the initial state at 0 hour; (**b**) shows the control group treated with PBS after 24 hours; (**c**) illustrates the effect of HP-PLLA at a concentration of 0.25 μg/μL after 24 hours; (**d**) depicts the impact of HP-PLLA at 0.50 μg/μL after 24 hours; (**e**) demonstrates the influence of HP-PLLA at 0.75 μg/μL after 24 hours; (**f**) represents the effect of HP-PLLA at the highest concentration of 1.00 μg/μL after 24 hours.

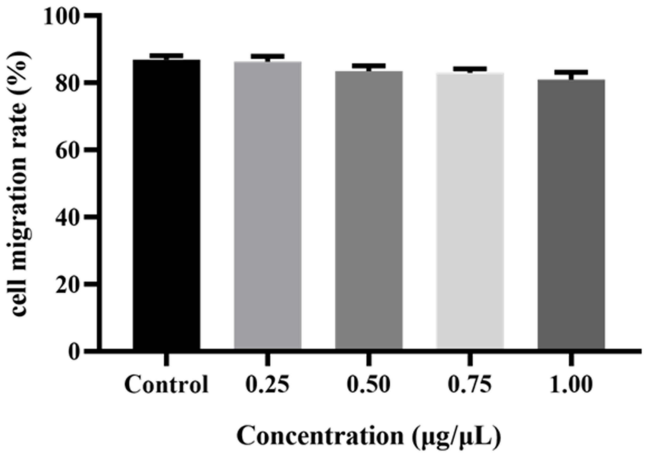

Figure 10 Cell migration rate of C6 cells following 24 hours incubation with different HP-PLLA concentrations. The migration rates are expressed as percentages and are plotted against the different HP-PLLA concentrations (0.25, 0.50, 0.75, 1.00 μg/μL).

revealed no significant difference (p>0.05) between the groups. Overall, the results indicated that HP-PLLA had no significant inhibitory effect on C6 cell migration.

Blood Biochemistry Analysis

To evaluate the in vivo toxicity of SA/PFP@HP-PLLA NPs, blood samples were collected from rabbits before and after NPs administration through cardiac blood sampling for biochemical and hematological assays. The results of the study were presented in Figure 11. No significant difference (p > 0.05) was observed in the comparison of all liver function indices (TP, ALB, GLB, ALT, AST) (a, b) and kidney function indices (BUN, CRE) (c) before and after administration, indicating that SA/PFP@HP-PLLA NPs had no significant hepatotoxicity and nephrotoxicity. These findings suggest that HP-PLLA has good biocompatibility.

Ultrasound Imaging Research in vitro

Perfluoropentane (PFP), a liquid that transitions to the gas phase upon exposure to ultrasound radiation or elevated temperature, undergoes acoustic droplet vaporization (ADV). This process promotes the aggregation of nanoparticles at tumor sites, enhancing ultrasound imaging efficiency. In this study, PFP was encapsulated within an amphiphilic block copolymer HP-PLLA carrier to formulate nanoparticles, creating a core-shell structure. These nanoparticles were then immersed in a water bath maintained at a constant temperature for experiments. The initial temperature of the water was set at 23°C and gradually

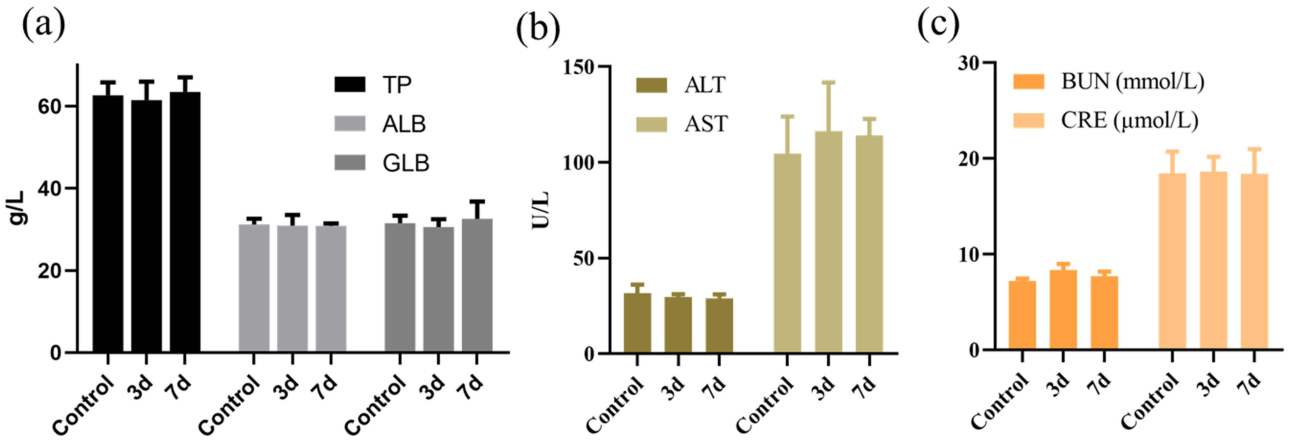

Figure 11 Blood biochemical analysis of normal rabbits before (control) and after (3d, 7d) injection of SA/PFP@HP-PLLA NPs. (**a** and **b**) liver function indices (TP, ALB, GLB, ALT, AST). (**c**) kidney function indices (BUN and CRE).

increased to 39°C in 2°C intervals, and ultrasound images were acquired using a 10 MHz probe positioned near the latex glove. The results were shown in Figure 12a and b. With increasing temperature and ultrasonic radiation time, the number of bright spots gradually rose, peaking at 35°C, before gradually decreasing. This observation suggests that the NPs undergo ADV in response to both ultrasound radiation and temperature increase.

Figure 12c displays an ultrasound image of saline, ultrasound medical coupling gel, and SA/PLLA-HP NPs in latex gloves immersed in a constant-temperature water bath at 37°C. Many bright spots reflecting the harmonic signals were observed in the ultrasound images of SA/PLLA-HP NPs, while no signals were detected in the ultrasound images of saline and ultrasound medical coupling gel. These results indicate that SA/PFP@HP-PLLA NPs possess specific acoustic properties that render them use for ultrasonography.

Ultrasound Imaging Research in vivo

Under ultrasound radiation, the nanoparticles unceasingly absorb energy from both positive and negative waves, resulting in compression and expansion movement, which produce a large number of harmonic signals. While in vivo tissues hardly produce harmonic signals, these differences in signals can be distinguished by some pulse sequences to enhance the imaging contrast. Figure 13 demonstrates the ultrasonographic imaging effect of nanoparticles on tumors in vivo. Compared to the pre-injection Figure 13a, the post-injection image Figure 13b exhibits brightness and distinct borders with the surrounding tissue, showing numerous bright spots throughout the tumor tissue. These changes result from the harmonic signal generated by the vaporization of nanobubble-encapsulated PFP in the presence of ultrasound waves, leading to visible ultrasonographic enhancement throughout the subcutaneous tumor.

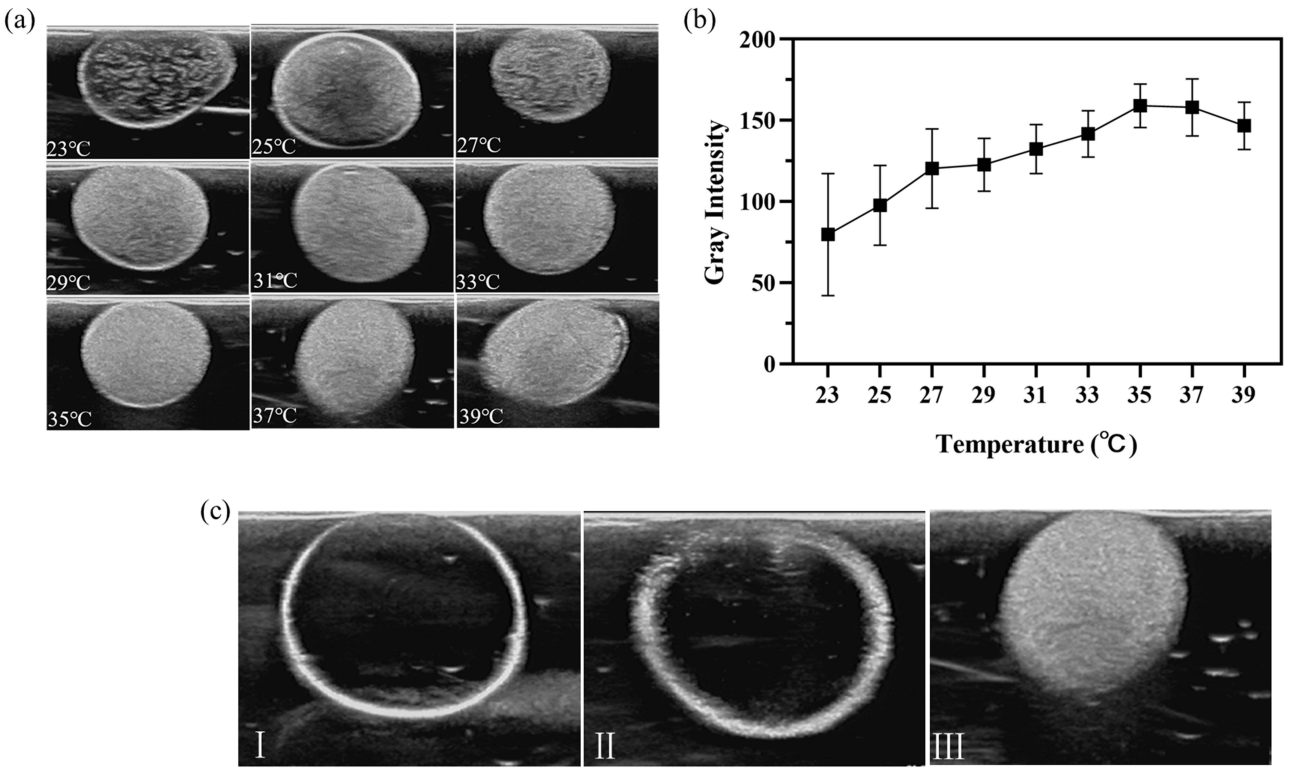

Figure 12 (**a**) The in vitro ultrasound images of SA/PFP@HP-PLLA NPs in latex glove mold. As the temperature increases from 23°C to 39°C at 2°C intervals, the number of bright spots in the images gradually increases. (**b**) Representative in vitro ultrasonic images and quantitative gray scale analysis of SA/PFP@HP-PLLA NPs with ultrasonic intensity in the range of 23 ~ 39°C. (**c**) Represents in vitro ultrasonic images obtained at a water bath temperature of 37°C. I Saline, II ultrasonic medicinal coupling gel, III SA/PFP@HP-PLLA NPs under high frequency diagnostic ultrasound in latex gloves mold.

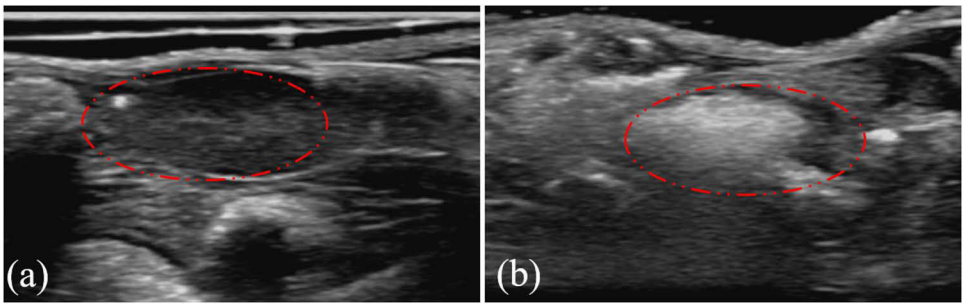

Figure 13 Ultrasound images of the subcutaneous tumor (red circles) in BALB/c nude mice, (**a** and **b**) are before and after injection of SA/PFP@HP-PLLA NPs.

In vitro CEST MRI

The CEST signal generation relied on the salicylic acid structure, where the phenol proton readily formed strong hydrogen bonds with the carboxylic acid anion. The electron cloud density of the benzene ring also influenced this process, enhancing the de-shielding effect on the phenol proton and producing a CEST contrast at approximately 9.3 ppm away from water.[29] Both Z-spectra Figure 14a and CEST image data Figure 14b revealed a concentration-dependent relationship between SA@HP-PLLA NPs and the CEST effect. Higher salicylic acid nanoparticle concentrations led to greater CEST enhancement. Furthermore, SA/PFP@HP-PLLA NPs exhibited sharper peaks compared to nanoparticles at the same concentration, as shown in Figure 14c and d. The magnitude of the CEST signal was influenced by the number of exchangeable protons.[35] It was speculated that the fluoride ion in PFP might bind to the carboxylic acid hydrogen protons in salicylic acid to form intermolecular hydrogen bonds, resulting in an overall molecular weight increase for salicylic acid and a corresponding increase in the total number of exchangeable protons, ultimately leading to an enhanced CEST signal.

The CEST spectra observed were influenced by imaging parameters and the tissue microenvironment. To optimize the CEST effect, we conducted a screening process on a phantom, evaluating the saturation power and pulse duration of the irradiated RF pulses. The results demonstrated a positive correlation between the CEST effect of SA/PFP@HP-PLLA NPs and increasing saturation power within a certain range Figure 15a and b. Similarly, the CEST effect of SA/PFP@HP-

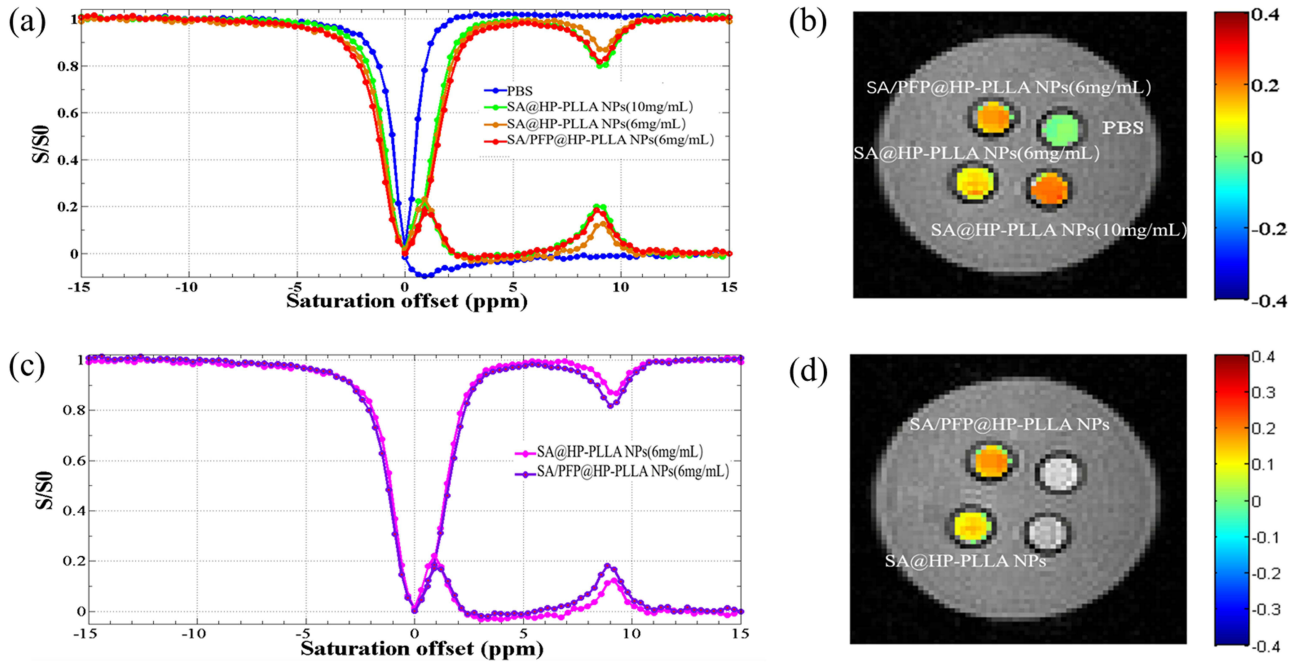

Figure 14 (**a**) Z-spectra and the corresponding CEST image (**b**) of various nanoparticle concentrations: 10 mg/mL SA@HP-PLLA NPs, 6 mg/mL SA@HP-PLLA NPs, 6 mg/mL SA/PFP@HP-PLLA NPs and PBS as a control. Additionally, (**c**) compares the Z-spectra and CEST image of SA@HP-PLLA NPs and SA/PFP@HP-PLLA NPs containing the same concentration of salicylic acid, with (**d**) providing a closer look at their CEST images.

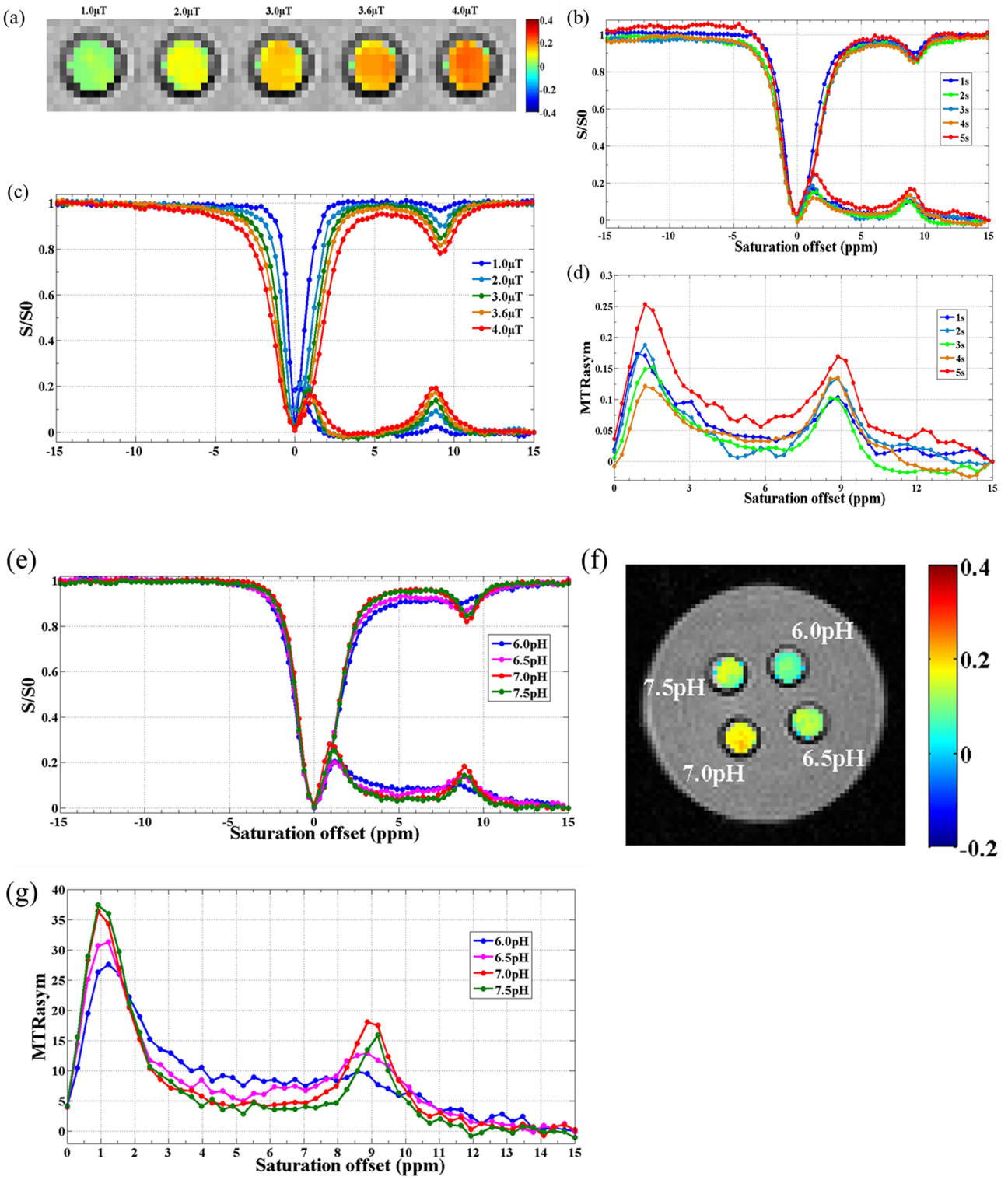

Figure 15 In vitro CEST characterizations of SA/PFP@HP-PLLA NPs at room temperature. The saturation power-dependence is shown in (**a**) Z-spectra and (**b**) for the corresponding CEST image. The saturation time-dependence is explored in (**c**) for Z-spectra and (**d**) for MTRasym spectra at pH 7.0 using a saturation power value of 3.6 μT. Furthermore, the pH-dependence examined in (**e**) for Z-spectra, (**f**) for the CEST image, and (**g**) for MTRasym spectra, using a saturation power value of 3.6 μT for 3s.

PLLA NPs generally increased with longer saturation time, up to a certain limit Figure 15c and d. Based on the physiological conditions and scanner hardware settings, we selected an optimal saturation power of 3.6 μT and a saturation time of 3 seconds for in vivo imaging research respectively. Under these optimized conditions, we further

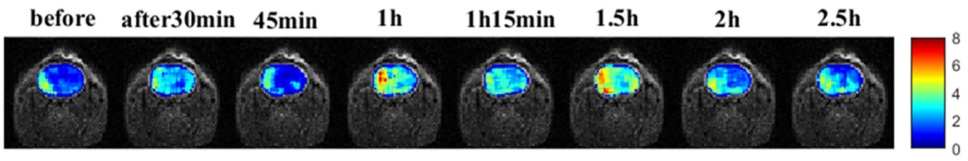

Figure 16 CEST imaging of rat brain SA/PFP@HP-PLLA NPs gliomas post injection. This figure illustrates CEST imaging results of rat brain gliomas before and after the injection of SA/PFP@HP-PLLA NPs at various time points. The CEST signal is shown to peak at approximately 90 minutes post-injection, followed by a gradual decrease. Notably, a significant attenuation in the CEST signal is observed 45 minutes after injection.

investigated the dependence of the CEST signal of SA/PFP@HP-PLLA NPs on PH. The CEST signal of SA/PFP@HP-PLLA NPs showed a trend of increasing and then decreasing within the range of pH 6.0~7.5 Figure 15e–g. Consequently, the optimal pH value was determined to be 7.0, consistent with a previous study by Yang et al.[29] These findings are crucial for understanding the optimal conditions for imaging using SA/PFP@HP-PLLA NPs and their application in physiological environments.

In vivo CEST Imaging

To assess the feasibility of SA/PFP@HP-PLLA NPs for CEST imaging of tumors in vivo, MRI experiments were conducted on rats bearing C6 gliomas. Prior to the injection of SA/PFP@HP-PLLA NPs, a baseline MTRasym value of approximately 2% was observed, presumably due to the existence of endogenous metabolites with hydroxy protons, such as glucose and inositol, within the brain tissue.[36] Post-injection of SA/PFP@HP-PLLA NPs, the CEST signal reached its peak at approximately 1.5 hours and gradually declined. Notably, a significant decrease in the CEST signal was observed 45 min after injection (Figure 16). This unexpected attenuation may stem from the intricate vascular network and blood circulation within the tumor, necessitating further investigation to elucidate the precise mechanism.

Conclusion

In this study, we successfully synthesized hematoporphyrin dihydrochloride-poly (lactic acid) (HP-PLLA) polymer and encapsulated SA/PFP into nanoparticles using the emulsion-solvent evaporation method. These nanoparticles exhibited uniform particle size, good stability, low cytotoxicity, and good biocompatibility. They also generated strong ultrasound and CEST MRI signals, significantly enhancing tumor visualization. Our findings suggest that SA/PFP@HP-PLLA NPs have great potential as a dual-modality imaging agent for preclinical and clinical applications, particularly in improving tumor boundary delineation and real-time treatment monitoring.

Acknowledgments

This work was supported by Hubei Provincial Natural Science Foundation of China (grant no. 2022CFB960); Scientific research and development funds of Hubei University of Science and Technology (grant no. 2022-24GP01); and Science and Technology Plan Project (in the field of Medical and Health Care) of Xiangyang (grant no. 2022YL15A).

Disclosure

The authors report no conflicts of interest in this work.

References

1. Xu H, Zong H, Ma C, et al. Evaluation of nano-magnetic fluid on malignant glioma cells. *Oncol Lett*. 2017;13(2):677–680. doi:10.3892/ol.2016.5513
2. Xu X, Liu K, Wang Y, et al. A multifunctional low-generation dendrimer-based nanoprobe for the targeted dual mode MR/CT imaging of orthotopic brain gliomas. *J Mat Chem B*. 2019;7(23):3639–3643. doi:10.1039/c9tb00416e
3. Junn JC, Soderlund KA, Glastonbury CM, et al. Imaging of head and neck cancer with CT, MRI, and US. *Semin Nucl Med*. 2021;51(1):3–12. doi:10.1053/j.semnuclmed.2020.07.005
4. Kyrkou SG, Vrettos EI, Gorpas D, et al. Design principles governing the development of theranostic anticancer agents and their nanoformulations with photoacoustic properties. *Pharmaceutics*. 2022;14(2):362. doi:10.3390/pharmaceutics14020362
5. Gao Z, Lu Q, Yan J. Value of differential diagnosis of contrast-enhanced ultrasound in benign and malignant thyroid nodules with microcalcification. *Oncol Lett*. 2019;17(5):4545–4549. doi:10.3892/ol.2019.10107

6. Sun X, Guo L, Shang M, et al. Ultrasound mediated destruction of LMW-HA-loaded and folate-conjugated nanobubble for TAM targeting and reeducation. *Int j Nanomed*. 2020;15:1967–1981. doi:10.2147/IJN.S238587
7. Yang Y, Li Q, Guo X, et al. Mechanisms underlying sonoporation: interaction between microbubbles and cells. *Ultrason Sonochem*. 2020;67:105096. doi:10.1016/j.ultsonch.2020.105096
8. Sugumaran S, Jamlos MF, Ahmad MN, et al. Nanostructured materials with plasmonic nanobiosensors for early cancer detection: a past and future prospect. *Biosens Bioelectron*. 2018;100:361–373. doi:10.1016/j.bios.2017.08.044
9. Abenojar EC, Bederman I, Leon AC, et al. Theoretical and experimental gas volume quantification of micro- and nanobubble ultrasound contrast agents. *Pharmaceutics*. 2020;12(3):1–12. doi:10.3390/pharmaceutics12030208
10. Li Y, Liu R, Liu L, et al. Study on phase transition and contrast-enhanced imaging of ultrasound-responsive nanodroplets with polymer shells. *Colloids Surf B*. 2020;189:110849. doi:10.1016/j.colsurfb.2020.110849
11. Perera RH, de Leon A, Wang X, et al. Real time ultrasound molecular imaging of prostate cancer with PSMA-targeted nanobubbles. *Nanomedicine*. 2020;28:102213. doi:10.1016/j.nano.2020.102213
12. Lan M, Zhu L, Wang Y, et al. Multifunctional nanobubbles carrying indocyanine green and paclitaxel for molecular imaging and the treatment of prostate cancer. *J Nanobiotechnol*. 2020;18(1):121. doi:10.1186/s12951-020-00650-1
13. Peng Y, Zhu L, Wang L, et al. Preparation of nanobubbles modified with a small-molecule CXCR4 antagonist for targeted drug delivery to tumors and enhanced ultrasound molecular imaging. *Int j Nanomed*. 2019;14:9139–9157. doi:10.2147/IJN.S210478
14. Liu R, Tang J, Xu Y, et al. Bioluminescence imaging of inflammation in vivo based on bioluminescence and fluorescence resonance energy transfer using nanobubble ultrasound contrast agent. *ACS nano*. 2019;13(5):5124–5132. doi:10.1021/acsnano.8b08359
15. Zhang Y, Wan CF, Du J, et al. The in vitro study of Her-2 targeted gold nanoshell liquid fluorocarbon poly lactic-co-glycolic acid ultrasound microcapsule for ultrasound imaging and breast tumor photothermal therapy. *J biomater sci Poly ed*. 2018;29(1):57–73. doi:10.1080/09205063.2017.1399003
16. Wang H, Ding L, Xu F, et al. Construction of novel amphiphilic chitosan-polylactide graft copolymer nanodroplets for contrast enhanced ultrasound tumor imaging. *J Biomater Appl*. 2021;36(4):1–13. doi:10.1177/08853282211011766
17. Xiao R, Zhao Z, Chen J, et al. Preparation and ultrasonic imaging investigation of perfluoropentane-filled polylactic acid nanobubbles as a novel targeted ultrasound contrast agent. *Front Mater*. 2020;7:1–7. doi:10.3389/fmats.2020.549002
18. Shin JE, Ogunyankin MO, Zasadzinski JA. Perfluoroheptane-loaded hollow gold nanoshells reduce nanobubble threshold flux. *Small*. 2019;15(7): e1804476. doi:10.1002/smll.201804476
19. Xavierselvan M, Cook J, Duong J, et al. Photoacoustic nanodroplets for oxygen enhanced photodynamic therapy of cancer. *Photoacoustics*. 2022;25:100306. doi:10.1016/j.pacs.2021.100306
20. Ward KM, Aletras AH, Balaban RS. A new class of contrast agents for MRI based on proton chemical exchange dependent saturation transfer (CEST). *J Magn Reson*. 2000;143(1):79–87. doi:10.1006/jmre.1999.1956
21. Poblador Rodriguez E, Moser P, Auno S, et al. Real-time motion and retrospective coil sensitivity correction for CEST using volumetric navigators (vNavs) at 7T. *Magn Reson Med*. 2021;85(4):1909–1923. doi:10.1002/mrm.28555
22. Han X, Huang J, Akw T, et al. CEST MRI detectable liposomal hydrogels for multiparametric monitoring in the brain at 3T. *Theranostics*. 2020;10 (5):2215–2228. doi:10.7150/thno.40146
23. Chen YW, Liu HQ, Wu Q, et al. pH mapping of skeletal muscle by Chemical Exchange Saturation Transfer (CEST) imaging. *Cells*. 2020;9 (12):1–15. doi:10.3390/cells9122610
24. Ngen EJ, Artemov D. Advances in monitoring cell-based therapies with magnetic resonance imaging: future perspectives. *Int J Mol Sci*. 2017;18 (1):26. doi:10.3390/ijms18010198
25. Consolino L, Anemone A, Capozza M, et al. Non-invasive investigation of tumor metabolism and acidosis by MRI-CEST imaging. *Front Oncol*. 2020;10:161. doi:10.3389/fonc.2020.00161
26. Zhu W, Chu C, Kuddannaya S, et al. In Vivo imaging of composite hydrogel scaffold degradation using CEST MRI and two-color NIR imaging. *Adv Funct Mater*. 2019;29(36):1–10. doi:10.1002/adfm.201903753
27. Jia Y, Geng K, Cheng Y, et al. Nanomedicine particles associated with chemical exchange saturation transfer contrast agents in biomedical applications. *Front Chem*. 2020;8:326. doi:10.3389/fchem.2020.00326
28. Jia Y, Chen Y, Geng K, et al. Glutamate Chemical Exchange Saturation Transfer (GluCEST) magnetic resonance imaging in pre-clinical and clinical applications for encephalitis. *Front Neurosci*. 2020;14:750. doi:10.3389/fnins.2020.00750
29. Yang X, Song X, Li Y, et al. Salicylic acid and analogues as diaCEST MRI contrast agents with highly shifted exchangeable proton frequencies. *Angew Chem Int Ed*. 2013;52(31):8116–8119. doi:10.1002/anie.201302764
30. Li B, Li Q, Mo J, Dai H. Drug-loaded polymeric nanoparticles for cancer stem cell targeting. *Front Pharmacol*. 2017;8:1–12. doi:10.3389/ fphar.2017.00051
31. Nanaki SG, Spyrou K, Bekiari C, et al. Hierarchical porous carbon-PLLA and PLGA hybrid nanoparticles for intranasal delivery of galantamine for alzheimer's disease therapy. *Pharmaceutics*. 2020;12(3):1–22. doi:10.3390/pharmaceutics12030227
32. Yang X, Song X, Ray Banerjee S, et al. Developing imidazoles as CEST MRI pH sensors. *Contr Media Mol Imag*. 2016;11(4):304–312. doi:10.1002/cmmi.1693
33. Luo B, Wang S, Rao R, et al. Conjugation magnetic PAEEP-PLLA nanoparticles with lactoferrin as a specific targeting MRI contrast agent for detection of brain glioma in rats. *Nanoscale Res Lett*. 2016;11(1):227–238. doi:10.1186/s11671-016-1421-x
34. Wang C, Du F. Preparation, characterization, and sonodynamic antitumor effect of the folate receptor targeted FA-EN-β-CD containing hemato-porphyrin in vitro. *Drug Dev Res*. 2020;81(5):585–592. doi:10.1002/ddr.21657
35. Ni D, Shen Z, Zhang J, et al. Integrating anatomic and functional dual-mode magnetic resonance imaging: design and applicability of a bifunctional contrast agent. *ACS nano*. 2016;10(3):3783–3790. doi:10.1021/acsnano.6b00462
36. Bagga P, Wilson N, Rich L, et al. Sugar alcohol provides imaging contrast in cancer detection. *Sci Rep*. 2019;9(1):9. doi:10.1038/s41598-019-47275-5